C23-86/51

MICROSCOPIC RELATIVISTIC DESCRIPTION OF PROTON–NUCLEUS SCATTERING

D. P. Murdock
and
C. J. Horowitz

Center for Theoretical Physics
and Department of Physics
Massachusetts Institute of Technology
Cambridge, Massachusetts 02139 USA

Submitted to: *Physical Review C*

CTP # 1366

July 1986

MICROSCOPIC RELATIVISTIC DESCRIPTION OF PROTON–NUCLEUS SCATTERING

D. P. Murdock and C. J. Horowitz

ABSTRACT

Relativistic microscopic calculations are presented for proton elastic scattering from ^{12}C, ^{16}O, ^{40}Ca, ^{48}Ca, ^{90}Zr, and ^{208}Pb at laboratory kinetic energies near 200 MeV. The calculations go beyond the original relativistic impulse approximation to include: (a) medium modifications from Pauli blocking; (b) the resolution of ambiguities in the relativistic NN amplitude by using pseudovector πN coupling; and, (c) an explicit treatment of exchange terms in the optical potential. The results quantitatively reproduce all measured spin observables (both analyzing power and spin rotation function) except at very large angles. The energy dependence and sensitivities are discussed.

I. INTRODUCTION

Recently there has been considerable interest in relativistic descriptions of proton–nucleus scattering. Relativistic impulse approximation (RIA)[2,3] calculations have provided a remarkably good description of elastic spin observables at laboratory kinetic energies, $T_{\rm lab}$ of 500 MeV and above.

These calculations are dramatic improvements on nonrelativistic results. The RIA calculations and their success have raised a number of questions. What are the essential aspects of relativity and to what extent are they included in conventional calculations? Clearly, there must be many corrections to the very simple impulse approximation. What role do they play? For example, von Geramb[1] has suggested that medium modifications to the NN interaction (omitted in the original RIA) provide important corrections to *non*relativistic calculations.

To address these questions, we have carried out an extensive series of microscopic relativistic elastic scattering calculations at $T_{\rm lab}$ near 200 MeV and above. The 200 MeV energy region is interesting for a variety of reasons. First, the original RIA fails at these low energies. We believe this failure is due to (among other things) ambiguities in the relativistic form of the NN interaction used. By performing calculations at low energies where the ambiguities are large we hope to gain insight into the relativistic nature of the interaction.

Second, medium modifications from Pauli blocking are important at these low energies. Therefore, calculations here allow one to examine their role in a relativistic approach and compare to medium modifications in nonrelativistic calculations.

Finally, there is new data for the spin rotation function Q near 200 MeV. This, together with A_y and $\frac{d\sigma}{d\Omega}$ already measured, allows one to compare theory with extensive and accurate complete sets of elastic scattering observables.

Any complex theoretical calculation will involve a number of approximations. To minimize any implicit (accidental?) adjustments of approximations to data, we have chosen to adopt a standard computational procedure and compare it systematically to the world supply of elastic data. (Note, no parameters in our calculations are explicitly adjusted to fit the nucleon–nucleus data.)

We consider all closed shell nuclei, ^{16}O, ^{40}Ca, ^{48}Ca, ^{90}Zr and ^{208}Pb, except ^{4}He (because of its large center of mass corrections). In addition, we consider ^{12}C because there is extensive data, including new Q measurements. We find that our relativistic calculations provide an excellent quantitative description of all elastic spin observables except at very large angles where there may be coupled channel effects.

The original RIA[2,3] involves two important steps. First, the experimental NN amplitudes are represented by a standard set of five Lorentz covariants[4] which we will refer to as the McNeil–Ray–Wallace (MRW) set. Then the Lorentz covariants are folded with nuclear densities to produce a first order "$t\rho$" optical potential for use in a Dirac equation.

The form of the Lorentz covariants chosen for the NN amplitudes involves important implicit dynamical assumptions about the relativistic NN interaction. Furthermore, this choice is ambiguous[5].

In addition, the standard MRW form has a very definite (somewhat awkward) behavior under the interchange of two particles (Fierz transformation)[6]. This behavior leads to problems for the simple RIA in handling exchange terms in nucleon–nucleus scattering. These problems grow more serious at lower energies and larger scattering angles.

Finally, the RIA assumes the NN interaction is unmodified in the medium. From extensive nonrelativistic calculations (for example, Ref. [1]) it is believed there are large modifications of the NN interaction from Pauli blocking and binding energy corrections. These modifications become very important at low energies where they substantially reduce the imaginary optical potential.

These theoretical limitations of the simple RIA show up in a number of ways. First, predictions for spin observables are much worse at $T_{\rm lab} = 200$ MeV than at 500 MeV and above[7]. Next, attempts to extract neutron densities using the RIA show large energy dependence at low energies[7]. Finally, large angle analyzing power data in Pb disagree strongly with the violent oscillations predicted by the simple RIA (with a naïve extrapolation of the amplitudes)[8].

Therefore, the present calculations include important physics beyond the original RIA prescription. First, explicit exchange terms are described with a simple direct plus exchange model of the NN amplitudes[6] which is discussed in Section II. This model greatly improves the description of large angle scattering. Furthermore, the model improves the treatment of the large exchange contributions of the pion to the scalar and vector invariants.

Next, ambiguities in the form of the NN interaction are resolved by using a pseudo*vector* ($\not{q}\gamma^5$, where q is the momentum transfer) rather than a pseudo*scalar* (γ^5) coupling for the pion. This choice is dictated by chiral symmetry and serves to greatly reduce both the strength and energy dependence of the real optical potential at low energies. Tjon and Wallace[9] have also examined these ambiguities in the interaction.

Finally, medium modifications from Pauli blocking are included. Relativistic Brueckner calculations for infinite nuclear matter are used to correct optical potentials for finite nuclei by using a simple local density approximation.

The formalism for our calculations is presented in Section II. Basically, our simple Direct + Exchange model of the NN interactions[6] is folded with relativistic mean field target densities[10] and then Pauli blocking corrections are applied. Section III presents results for differential cross sections, analyzing powers, spin rotation functions and reaction cross sections for $T_{\rm lab}$ near 200 MeV. Here we discuss the differences between Pauli blocked and free calculations and between pseudoscalar and pseudovector versions of the NN interaction.

The sensitivities of the calculation to changes in densities, treatments of exchange, etc. are investigated in Section III.C. An explicit treatment of exchange is important in describing the new large angle analyzing power data in Pb[11]. Finally, the energy dependence of the calculations is examined in Section III.D. Here, 400 MeV calculations for Pb show that Pauli blocking is much reduced. Furthermore, there is almost no difference between pseudovector and pseudoscalar amplitudes at this energy. Thus, our calculations reduce to the original RIA results as the energy is increased to 500 MeV and above.

In Section VI, we conclude that our extensions to the RIA allow one to systematically reproduce all elastic spin observables near 200 MeV. We end by discussing future work, looking at other ambiguities in the relativistic interaction and extending the calculations to energies below 200 MeV.

II. FORMALISM

A. RELATIVISTIC IMPULSE APPROXIMATION

Many theoretical works have suggested the reaction cross section for proton–nucleus scattering is dominated by single–nucleon knockout. This suggests that some kind of a "$t\rho$" optical potential where an NN interaction in the medium is folded with a ground state density is a good starting point. Note, any relativistic $t\rho$ approximation for elastic scattering may have definite implications for the spin observables in quasielastic (where the excitation energy is approximately $q^2/2M$ for momentum transfer q) proton–nucleus scattering[12].

In this paper we wish to focus on relativistic aspects of a $t\rho$ approximation. First, the optical potential U is assumed to be a 4×4 matrix in the Dirac spinor space of the projectile. This matrix has important scalar U^S and vector U^V pieces:

$$U_{\rm opt} = U^S + \gamma_0 U^V \tag{2.1}$$

where our gamma matrices and metric are those of Bjorken and Drell[13].

Next, the NN interaction t is assumed to be a $4 \times 4 \otimes 4 \times 4$ matrix in the spinor spaces of the two particles. The original RIA inferred this complete matrix from on–shell NN scattering phase shifts *and* important implicit assumptions about the matrix form of t.

McNeil, Ray and Wallace[4] equated on–shell matrix elements of a $4 \times 4 \otimes 4 \times 4$ matrix $\hat{\mathcal{F}}$ to the experimental NN amplitudes. The on–shell amplitudes in the NN center of mass frame can be written[4]:

$$(2ik_c)^{-1} f_c = A + B\sigma_1 \cdot \sigma_2 + iqC(\sigma_{1n} + \sigma_{2n}) + D\sigma_1 \cdot q\, \sigma_2 \cdot q + E\sigma_{1x}\sigma_{2x} \qquad (2.2)$$

Here k_c is the momentum in the center of mass frame, f_c is the nonrelativistic scattering amplitude (normalized so the cross section is $|f_c|^2$) and A, B, C, D and E are Wolfenstein amplitudes which describe the spin dependence of the NN interaction. Here for example, σ_{1n} is a 2×2 Pauli matrix (in the direction normal to the plane) for particle one. The Pauli spinor χ_i matrix elements of Eq. (2.2) are equated to Dirac spinor matrix elements of the relativistic amplitude $\hat{\mathcal{F}}$:

$$(2ik_c)^{-1} \chi^\dagger_{s_1'} \chi^\dagger_{s_2'} f_c(E,q) \chi_{s_1} \chi_{s_2} = \bar{U}(\vec{k}_c', s_1') \bar{U}(-\vec{k}_c', s_2') \hat{\mathcal{F}}(E_c, q) U(\vec{k}_c, s_1) U(-\vec{k}_c, s_2) \ . \qquad (2.3)$$

Here, $U(k_c, s_1)$ is a free 4–component Dirac spinor of spin projection s_1 (normalized so that $\bar{U}\, U = 1$):

$$U(k_c, s_1) = \sqrt{\frac{E_c + M}{2M}} \begin{pmatrix} 1 \\ \frac{\vec{\sigma} \cdot \vec{k}_c}{E_c + M} \end{pmatrix} \chi_{s_1} \qquad (2.4)$$

The momenta and spins of the interacting nucleons before the collision are $\vec{k}_c, s_1$: $-\vec{k}_c, s_2$; $q = |\vec{k}' - \vec{k}|$ and the energy E_c is $E_c = \sqrt{k_c^2 + M^2}$. Isospin labels are omitted, although we will be interested in pp and pn scattering, with the corresponding relativistic amplitudes $\hat{\mathcal{F}}_{pp}$ and $\hat{\mathcal{F}}_{pn}$. The amplitude $\hat{\mathcal{F}}(E, q)$ is a Dirac operator in the Hilbert space of the two particles. We will abbreviate the right side of (2.3) as $\bar{U}_1 \bar{U}_2 \hat{\mathcal{F}} U_1 U_2$.

Equation (2.3) only determines a small subset of the 256 components in $\hat{\mathcal{F}}$. Isospin and parity reduce the number of independent spin matrix elements in Eq. (2.2) to five (for example the $A \ldots E$). There will be an infinite number of operators $\hat{\mathcal{F}}$ with the same five on–shell matrix elements, but different $4 \times 4 \otimes 4 \times 4$ matrix structures. These different structures will give, for example, different negative energy spinor matrix elements of $\hat{\mathcal{F}}$. These ambiguities are important because we will use the full $\hat{\mathcal{F}}$, not just $\bar{U}_1 \bar{U}_2 \hat{\mathcal{F}} U_1 U_2$ to construct an optical potential.

The information contained in the measurement of the NN amplitudes at a given energy– which gives the five complex Wolfenstein parameters– is not sufficient to determine the operator $\hat{\mathcal{F}}$ completely, so without further theoretical input, assumptions need to be made about the form of $\hat{\mathcal{F}}(q)$. These assumptions will determine the behavior of the NN amplitudes as the spinors U change. The choice for $\hat{\mathcal{F}}(q)$ made in the original RIA was:

$$\hat{\mathcal{F}}(q, E) = \sum_L F^L(q, E) \lambda^L_{(1)} \cdot \lambda^L_{(2)} \qquad (2.5)$$

where the L's stand for the Dirac matrix types listed in Table I. For example, the tensor term contributes $F^T(q, E) \bar{U}_1 \sigma^{\mu\nu} U_1 \, \bar{U}_2 \sigma_{\mu\nu} U_2$. With this form, one can derive a 5×5 nonsingular matrix relating the F^L to the 5 Wolfenstein parameters $A, \ldots, E$ [4]. We emphasize that only the free matrix elements of (2.5) are determined by the NN data while the "off–shell" operator is needed to construct an optical potential. Other assumptions for the form of $\hat{\mathcal{F}}$ are possible, in particular replacing γ^5 by $\not{q}\gamma^5$ which gives the same result for the amplitudes when operating on free spinors but which will give a different $t\rho$ optical potential.

TABLE I	
$\hat{\mathcal{F}} = \sum_L F^L(q, E)\, \lambda^L_{(1)} \cdot \lambda^L_{(2)}$	
L	λ^L
S (Scalar)	1
V (Vector)	γ_μ
P (Pseudoscalar)	γ_5
A (Axial-Vector)	$\gamma_5\gamma_\mu$
T (Tensor)	$\sigma_{\mu\nu}$

The Dirac optical potential is then given by[2,3]:

$$U_{\rm opt} = \frac{-4\pi i p_{\rm lab}}{M} \langle \bar{\psi}_2 | \hat{\mathcal{F}} | \psi_2 \rangle \qquad (2.6)$$

where $p_{\rm lab}$ is the laboratory momentum of the incident proton and $|\psi_2\rangle$ is the ground state wavefunction of the target nucleus, typically a (Hartree) product of single-particle 4-component wavefunctions ϕ_α, with the states labelled by α. For spherical nuclei, parity implies only the S, V, and T parts of $\hat{\mathcal{F}}$ contribute:

$$U_{\rm opt}(q) = \frac{-4\pi i p_{\rm lab}}{M} [F^S(q)\rho_S(q) + \gamma^0 F^V(q)\rho_V(q) - 2i\vec{\alpha} \cdot \hat{r} F^T(q)\rho_T(q)] \qquad (2.7)$$

where the target densities are the Fourier transforms of the r-space scalar, vector (baryon) and tensor densities. These are sums over the occupied nuclear levels:

$$\rho_S(r) = \sum_\alpha^{\rm occ} \bar{\phi}_\alpha \phi_\alpha \qquad (2.8a)$$

$$\rho_V(r) = \sum_\alpha^{\rm occ} \phi^\dagger_\alpha \phi_\alpha \qquad (2.8b)$$

$$[\hat{r}\rho_T(r)]^i = \sum_\alpha^{\rm occ} \bar{\phi}_\alpha \sigma^{0i} \phi_\alpha \ . \qquad (2.8c)$$

With this optical potential, the observables $\frac{d\sigma}{d\Omega}$, A_y, and Q for elastic scattering of protons from spin–0 nuclei are calculated by solving a Dirac equation (see Appendix B).

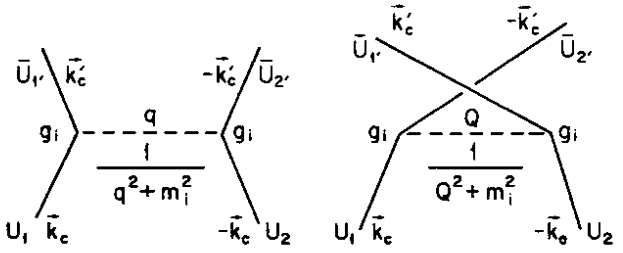

Fig. 1: Meson exchange diagrams for the relativistic Love–Franey model.

B. RELATIVISTIC LOVE–FRANEY MODEL

In Ref. [6] a model was presented which enables one to include exchange terms in the optical potential. These were only approximately treated in the original RIA but become increasingly important at lower energies. Also, this model allows one to examine ambiguities in the form of $\hat{\mathcal{F}}(q)$.

The NN amplitude is modeled as arising from the first Born approximation for the exchange of a set of "mesons" (see Fig. 1) whose parameters are fit to reproduce NN scattering data at separate energies. The mesons are of different Lorentz types (scalar, vector, tensor, pseudoscalar and axial vector) and isospins. The coupling constants are complex with a real coupling g_i^2 and an imaginary one $\bar{g}_i^2$. The small imaginary couplings are a purely phenomenological means of obtaining the imaginary amplitude. The mesons have propagators of the form $\frac{1}{q^2+m^2}$ and the meson-nucleon vertices have form factors $\frac{1}{1+\frac{q^2}{\Lambda^2}}$ with separate m and Λ for the real and imaginary contributions to the amplitude, denoted respectively by $m,\bar{m}$ and $\Lambda,\bar{\Lambda}$. The parameters found for the real amplitude have a close correspondence with those of one-boson exchange potential fits[14,15] to NN data.

To calculate the NN amplitudes we consider the diagrams in Fig. 1 where the two interacting nucleons are identical particles in either a $T=0$ or $T=1$ total isospin state. The NN–meson vertex factor from the Feynman rules is:

$$g_i\left(\frac{1}{1+\frac{q^2}{\Lambda_i^2}}\right)\lambda^{L(i)}(\vec{\tau})^{I_i} \tag{2.9}$$

where $L(i)$ denotes the Lorentz type of the i^{th} meson (see table I) and and $I_i=(0,1)$ is its isospin. The $T=0$ scattered wave is symmetric for space–spin interchange so there is a relative $(+)$ sign between diagrams $1a$ and $1b$. For $T=1$ scattering, the wavefunction is antisymmetric and likewise there is a relative minus sign. Then up to overall kinematic factors, the contribution of meson i to the amplitude is:

$$\bar{U}_{1'}\bar{U}_{2'}\hat{\mathcal{F}}^i U_1 U_2 \propto \frac{g_i^2}{m_i^2+q^2}\left(\frac{1}{1+\frac{q^2}{\Lambda_i^2}}\right)^2 \bar{U}_{1'}\lambda^{L(i)}U_1\ \bar{U}_{2'}\lambda^{L(i)}U_2\ \{\vec{\tau}_1\cdot\vec{\tau}_2\}^{I_i}$$
$$+(-1)^T\frac{g_i^2}{m_i^2+Q^2}\left(\frac{1}{1+\frac{Q^2}{\Lambda_i^2}}\right)^2 \bar{U}_{2'}\lambda^{L(i)}U_1\ \bar{U}_{1'}\lambda^{L(i)}U_2\ \{\vec{\tau}_1\cdot\vec{\tau}_2\}^{I_i} \tag{2.10}$$

where the "exchange momentum transfer" is $Q=|\vec{k}'+\vec{k}|$. $\lambda^{L(i)}\cdot\lambda^{L(i)}$ has the same meaning as given in Table I and there is also a contribution to the imaginary part with the same form.

The first term in (2.10) is already of the form given by Eqs. (2.3) and (2.5) from which we can identify the contributions to the F^L's. The second term is not of this form because of the different order of the spinors in the product. However, it can be rewritten with a Fierz transformation:

$$(\bar{U}_{2'}\lambda^L U_1)(\bar{U}_{1'}\lambda^L U_2)=\sum_{L'}c_{LL'}(\bar{U}_{1'}\lambda^{L'}U_1)(\bar{U}_{2'}\lambda^{L'}U_2) \tag{2.11}$$

where

$$c_{LL'}=\frac{1}{8}\begin{pmatrix} 2 & 2 & 1 & -2 & 2\\ 8 & -4 & 0 & -4 & -8\\ 24 & 0 & -4 & 0 & 24\\ -8 & -4 & 0 & -4 & 8\\ 2 & -2 & 1 & 2 & 2\end{pmatrix} \tag{2.12}$$

with rows and columns labelled in the order (S,V,T,A,P). So (2.10) becomes:

$$\bar{U}_{1'}\bar{U}_{2'}\hat{\mathcal{F}}^i U_1 U_2 \propto \frac{g_i^2}{m_i^2+q^2}\left(\frac{1}{1+\frac{q^2}{\Lambda_i^2}}\right)^2 \{\tau_1\cdot\tau_2\}^{I_i}\bar{U}_{1'}\lambda^{L(i)}U_1\bar{U}_{2'}\lambda^{L(i)}U_2$$
$$+(-1)^T\frac{g_i^2}{m_i^2+Q^2}\left(\frac{1}{1+\frac{Q^2}{\Lambda_i^2}}\right)^2 \{\tau_1\cdot\tau_2\}^{I_i}\sum_{L'}c_{L(i)L'}\bar{U}_{1'}\lambda^{L'}U_1\ \bar{U}_{2'}\lambda^{L'}U_2 \tag{2.13}$$

and the identification with the contributions to the invariants $F^S\ldots F^P$ can now be made. Note that while in the first ("direct") piece a meson always contributes to the F^L invariant of the same Lorentz type, this is not the case with the second ("exchange") term. For example, the pseudoscalar "meson", with $L(i)=P$ now contributes to the scalar invariant F^S because the Fierz matrix element $c_{P,S}$ is nonzero. So the "pion" of the model has an effect on the scalar optical potential from the exchange term.

With the spinor normalization used here, the kinematic factor needed in (2.13) to give the free spinor matrix element as in Eqs. (2.3) and (2.5) is $\frac{iM^2}{2E_c k_c}$. Collecting all

of these pieces, the total contribution to the invariant F^L from all of the N "mesons" is a sum of direct and exchange pieces:

$$F^L = i\frac{M^2}{2E_c k_c}[F_D^L(q) + F_{Ex}^L(Q)] \tag{2.14}$$

$$F_D^L = \sum_{i=1}^{N} \delta_{L,L(i)}\{\vec{\tau}_1 \cdot \vec{\tau}_2\}^{I_i} f^i(q) \tag{2.15a}$$

$$F_{Ex}^L = (-1)^T \sum_{i=1}^{N} c_{L(i),L}\{\vec{\tau}_1 \cdot \vec{\tau}_2\}^{I_i} f^i(Q) \tag{2.15b}$$

where

$$f^i(q) = f_R^i(q) - if_I^i(q)$$

$$f_R^i(q) = \frac{g_i^2}{q^2+m_i^2}\left(1+\frac{q^2}{\Lambda_i^2}\right)^{-2} \qquad f_I^i = \frac{\bar{g}_i^2}{q^2+\bar{m}_i^2}\left(1+\frac{q^2}{\bar{\Lambda}_i^2}\right)^{-2} \tag{2.16}$$

Finally, to get the invariant for pp and pn scattering.

$$F^L(pp) = F^L(T=1) \tag{2.17a}$$

$$F^L(pn) = \frac{1}{2}[F^L(T=1) + F^L(T=0)] \tag{2.17b}$$

Our procedure for calculating the optical potential for finite nuclei from these amplitudes will be given below.

We have examined the effect on the optical potential of using pseudovector coupling for the "pion" of this model, that is, replacing $\lambda^P = \gamma^5$ by $\lambda^P = \pm\frac{\not{k}\gamma^5}{2M}$. As noted above, this does not change the parameters obtained from the fit to the NN data because the free spinors U satisfy:

$$(\bar{U}_{1'}\gamma^5 U_1)(\bar{U}_{2'}\gamma^5 U_2) = -(\bar{U}_{1'}\frac{\not{k}\gamma^5}{2M}U_1)(\bar{U}_{2'}\frac{\not{k}\gamma^5}{2M}U_2) \tag{2.18a}$$

$$(\bar{U}_{2'}\gamma^5 U_1)(\bar{U}_{1'}\gamma^5 U_2) = -(\bar{U}_{2'}\frac{\not{Q}\gamma^5}{2M}U_1)(\bar{U}_{1'}\frac{\not{Q}\gamma^5}{2M}U_2) \tag{2.18b}$$

While the direct amplitude from λ^P still does not contribute to the optical potential, the new "off-shell" behavior of the exchange term will make a difference. We use the new form of the pseudoscalar amplitude, $\not{k}\gamma^5$, to calculate the contribution of the pion to the optical potential in symmetric nuclear matter. (Note the right hand side of Eq. (2.18b) is not of the form for the Fierz identity.)

$$U_{ex}^{pv} = \frac{4\pi p_{\rm lab}}{M}\left(\frac{M^2}{2E_c k_c}\right) f^P(Q)\left\{\sum_{\rm protons}^{\rm occ}\frac{\gamma^5\not{Q}}{2M}|\bar{U}_2\rangle\langle U_2|\frac{\gamma^5\not{Q}}{2M}\right.$$
$$\left. + 2\sum_{\rm neutrons}^{\rm occ}\frac{\gamma^5\not{Q}}{2M}|\bar{U}_2\rangle\langle U_2|\frac{\gamma^5\not{Q}}{2M}\right\} \tag{2.19}$$

$$U_{ex}^{pv} = \frac{4\pi p_{\rm lab}}{M}\left(\frac{M^2}{2E_c k_c}\right) f^P(Q)\frac{3}{2}\left\{\sum_{\rm nucleons}^{\rm occ}\frac{\gamma^5\not{Q}}{2M}|\bar{U}_2\rangle\langle U_2|\frac{\gamma^5\not{Q}}{2M}\right\} \tag{2.20}$$

To do the sum on the nucleon states in nuclear matter, we use spinors of effective mass $M^* = M - g_S\phi$. ϕ being the scalar field of the Walecka model[16] and where starred quantities use this effective mass. Note that now for the bound states, we use $\bar{U}_2 U_2 = \frac{M^*}{E^*}$ and $U_2^\dagger U_2 = 1$ as with the original RIA. Summing on spins for each momentum state,

$$\sum_{\rm spins}|\bar{U}_2\rangle\langle U_2| = \frac{\not{k}^* + M^*}{2E^*}\,, \tag{2.21}$$

$$U_{ex}^{pv} = \frac{4\pi p_{\rm lab}}{M}\left(\frac{M^2}{2E_c k_c}\right) f^P(Q)\left(\frac{3}{2}\right) 2\int_{k\le k_F}\frac{d^3k}{(2\pi)^3}\frac{\gamma^5\not{Q}}{2M}\frac{(\not{k}^*+M^*)}{2E^*}\frac{\gamma^5\not{Q}}{2M}$$
$$= \frac{4\pi p_{\rm lab}}{M}\left(\frac{M^2}{2E_c k_c}\right) f^P(Q)\left(\frac{3}{8}\right)\left\{4\int_{k\le k_F}\frac{\not{Q}}{2M}\frac{E^*\gamma_0 - M^*}{E^*}\frac{\not{Q}}{2M}\frac{d^3k}{(2\pi)^3}\right\} \tag{2.22}$$

Next, we assume k is small compared to $p_{\rm lab}$ (and make an impulse approximation).

$$U_{ex}^{pv} = \frac{4\pi p_{\rm lab}}{M}\left(\frac{M^2}{2E_c k_c}\right) f^P(Q)\left(\frac{3}{8}\right)\frac{1}{4M^2}\not{Q}[\gamma^0\rho_B - \rho_S]\not{Q} \tag{2.23}$$

The scalar and vector components can be projected out by taking traces, giving:

$$U_{ex}^{pv} = U_S^{pv} + \gamma_0 U_V^{pv} \tag{2.24a}$$

$$U_V^{pv} = \frac{4\pi p_{\rm lab}}{M}\left(\frac{M^2}{2E_c k_c}\right) f^P(Q)\left(\frac{3}{8}\right)\frac{(2Q_0^2 - Q_\mu^2)}{4M^2}\rho_B \tag{2.24b}$$

$$U_S^{pv} = \frac{4\pi p_{\rm lab}}{M}\left(\frac{M^2}{2E_c k_c}\right) f^P(Q)\left(\frac{3}{8}\right)\left(-\frac{Q_\mu^2}{4M^2}\right)\rho_S \tag{2.24c}$$

If instead, the γ^5 vertex choice (pseudoscalar coupling) is made, the results are:

$$U_V^{ps} = \frac{4\pi p_{\rm lab}}{M}\left(\frac{M^2}{2E_c k_c}\right) f^P(Q)\left(\frac{3}{8}\right)\rho_B \tag{2.25a}$$

$$U_S^{ps} = -\frac{4\pi p_{\rm lab}}{M}\left(\frac{M^2}{2E_c k_c}\right) f^P(Q)\left(\frac{3}{8}\right)\rho_S \tag{2.25b}$$

which can also come from using the Fierz transformation and then the original RIA with nuclear matter densities (ρ_B, ρ_S).

Comparison of (2.24) and (2.25) shows that the choice of the pseudovector invariant has reduced the contribution of the pi meson by a factor of $\approx \mp\frac{Q^2}{4M^2}$ for the $\binom{\rm scalar}{\rm vector}$ potential. Here we approximate Q_0, the change of energy of the struck particle, as being very small compared to the change in momentum. Thus, in calculating optical potentials, we insert this factor for the choice of pseudovector coupling. This factor is much less than 1 and its inclusion improves the behavior of the nuclear matter Dirac

optical potentials at low energy by making both scalar and vector potentials smaller in absolute value. See Ref. [6].

C. LOCAL-DENSITY APPROXIMATION

To form the r-space optical potential for a finite nucleus, we write F^S, F^V, and F^T in (2.14) as a sum of direct and exchange amplitudes:

$$F^i = t^i_D(q) + t^i_{Ex}(Q) \tag{2.26}$$

where $t^i_D = \frac{iM^2}{2E_c k_c} F^i_D$ and $t^i_{Ex} = \frac{iM^2}{2E_c k_c} F^i_{Ex}$. The contribution to the optical potential of the direct piece is the same as with the original RIA, namely (here, i = scalar, vector and tensor):

$$U^i_D(r,E) = \frac{-4\pi i p_{\rm lab}}{M} \int d\vec{r}' \rho^i(\vec{r}') t^i_D(|\vec{r}-\vec{r}'|, E) \tag{2.27}$$

where

$$t^i_{D,Ex}(r,E) = \int \frac{d\vec{q}}{(2\pi)^3} t_{D,Ex}(\vec{q}) e^{-i\vec{q}\cdot\vec{r}} \tag{2.28}$$

For the nonlocal exchange term we use the local density approximation of Brieva and Rook[17], which uses plane wave states for the incident and bound nucleons:

$$U^i_{Ex}(r,E) = \frac{-4\pi i p_{\rm lab}}{M} \int d\vec{r}' \rho^i(\vec{r},\vec{r}') t^i_{Ex}(|\vec{r}-\vec{r}'|, E) j_0(k|\vec{r}-\vec{r}'|) \tag{2.29}$$

Here, k is the free projectile momentum, $k = p_{\rm lab}$. (At $T_{\rm lab}$ near 200 MeV, changes in k due to the real part of the optical potential are very small.) The off–diagonal one body density $\rho^i(\vec{r},\vec{r}')$ is approximated by:

$$\rho^i(\vec{r},\vec{r}') \approx \rho^i(\frac{1}{2}(\vec{r}+\vec{r}')) \frac{3}{(sk_F)^3} [\sin(sk_F) - sk_F \cos(sk_F)] \tag{2.30}$$

where $s = |\vec{r}-\vec{r}'|$ and k_F is related to the baryon density $\rho_B(\frac{1}{2}(\vec{r}+\vec{r}')) = \frac{2}{3\pi^2} k_F^3$. A sum on proton densities with pp amplitudes and neutron densities with pn amplitudes is implied in Eqs. (2.27) and (2.29). The Dirac optical potential for the scattering calculations is

$$U^i(r,E) = U^i_D(r,E) + U^i_{Ex}(r,E)\ , \tag{2.31a}$$

and

$$U_{\rm opt} = U^S + \gamma^0 U^V - 2i\vec{\alpha}\cdot\hat{r} U^T \tag{2.31b}$$

(Note the factor of two in the tensor potential.) The r-space functions $t^i_D(r)$ and $t^i_{Ex}(r)$ require the following Fourier transforms:

$$\int \frac{d\vec{q}}{(2\pi)^3} e^{i\vec{q}\cdot\vec{r}} f(q) = \frac{g^2}{4\pi} \frac{\Lambda^2}{(\Lambda^2-m^2)} \left\{ \frac{\Lambda^2}{(\Lambda^2-m^2)} \frac{(e^{-mr}-e^{-\Lambda r})}{r} - \frac{\Lambda}{2} e^{-\Lambda r} \right\} \tag{2.32}$$

TABLE II				
	SCALAR		VECTOR	
Energy (MeV)	Real	Imag.	Real	Imag.
200	-0.008	0.098	0.061	0.207
400	-0.043	0.061	-0.012	0.089

Pauli Blocking Correction Factors a_i (see Eq. (2.35)).

where

$$f(q) = \frac{g^2}{q^2+m^2} \left(1 + \frac{q^2}{\Lambda^2}\right)^{-2} \tag{2.33}$$

and the exchange amplitude with pseudovector coupling has a $\frac{q^2}{4M^2}$ factor:

$$\int \frac{d\vec{q}}{(2\pi)^3} e^{i\vec{q}\cdot\vec{r}} \frac{q^2}{4M^2} f(q) = \frac{\Lambda^2}{4M^2} \frac{g^2}{4\pi} \frac{\Lambda^2}{(\Lambda^2-m^2)} \left\{ \frac{m^2}{(\Lambda^2-m^2)} \frac{(e^{-\Lambda r}-e^{-mr})}{r} + \frac{\Lambda}{2} e^{-\Lambda r} \right\} \tag{2.34}$$

D. PAULI BLOCKING CORRECTIONS

We now correct the optical potentials of Eq. (2.31) for medium modifications from Pauli blocking. Relativistic Brueckner theory calculations (similar to Ref. [18]) of $U_{\rm opt}$ have been performed for infinite nuclear matter. These calculations use the HEA[15] one-boson exchange potential and do not include binding energy (dispersion) corrections. The results with the Pauli exclusion operator, U_{pb} at various densities can be well represented by

$$U^i_{pb}(r) = \left[1 - a_i(T_{\rm lab}) \left(\frac{\rho_B(r)}{\rho_0}\right)^{\frac{2}{3}}\right] U^i(r) \tag{2.35}$$

Here, U^i is the optical potential calculated without the Pauli operator, and $\rho_0 = .1934\ fm^{-3}$. The approximate k_F^2 or $\rho_B^{\frac{2}{3}}$ density dependence agrees with phase space results for isotropic scattering. Therefore the nuclear matter calculations give Pauli blocking factors $a_i(T_{\rm lab})$ for each energy $T_{\rm lab}$. These are collected in Table II and are different for the real and imaginary parts of the scalar and vector potentials. (We omit Pauli blocking for the small tensor potential.)

At 200 MeV the imaginary potentials are Pauli blocked by about 10 percent while the change in the real potentials is smaller. Note, because a_i is different for i = scalar and vector, the effect on the Schrödinger equivalent imaginary potential, which involves cancellations (see Section III, Eq. (3.1a)) is larger.

We use these nuclear matter results in a local density approximation to correct our finite nucleus optical potentials. Potentials from (2.31) are simply multiplied as in Eq. (2.35), where the baryon density is taken to be the $\rho_B(r)$ of the target. We find that the $\frac{2}{3}$ exponent in Eq. (2.35) is not critical for the results in Section III.

In summary, our calculation of the Dirac optical potentials for p–A elastic scattering goes as follows: We use the relativistic Love-Franey parametrizations of Ref. [6] to calculate direct and exchange amplitudes $t_D(q)$ and $t_{Ex}(Q)$ through Eqs. (2.14)–(2.17) and (2.26). Then we fold these amplitudes with the relativistic Hartree densities of Ref. [10] using a local density approximation for the exchange part to get an optical potential. We then apply the correction factor of Eq. (2.35) to include Pauli blocking.

III. RESULTS

A. DIRAC POTENTIALS

Before presenting scattering observables, we look at the optical potentials in order to show the importance of some features of the model and compare with optical potentials from other approaches. In the last section it was noted how the scalar and vector optical potentials in nuclear matter decrease in strength when pseudovector pion coupling is used in place of pseudoscalar coupling. Fig. 2 shows the same effect for ^{90}Zr at 200 MeV. We have used pseudovector coupling only for the real part of the optical potential, being guided by known pion–nucleon interactions. For the imaginary part, we leave the original MRW amplitude alone and use a pseudoscalar invariant. (If a pseudovector imaginary potential is used instead, the changes in observables are very small.) The further effect of Pauli blocking is also shown.

In Fig. 3 we compare our relativistic optical potential for ^{40}Ca at 200 MeV, (using pseudovector coupling and including the Pauli correction) with a phenomenological Wood–Saxon fit to scattering data by Clark *et al.*[19]. The agreement is very good.

To compare our results with the optical potentials from nonrelativistic models, we calculate the "Schrödinger–equivalent" potentials which follow from the relativistic scalar and vector types. These are functions which play the same role as the nonrelativistic potential when the Dirac equation for the projectile is written as a second order equation for the upper components[19]. Ignoring the small tensor and Coulomb potentials, the relation between the nonrelativistic central U_c and spin–orbit U_{so} potentials and the relativistic ones is:

$$U_c \approx \frac{1}{2E}[2EU^V + 2MU^S - (U^V)^2 + (U^S)^2] + U_{\rm Darwin} \tag{3.1a}$$

$$U_{so} \approx \frac{1}{2E}\left[-\frac{1}{rA}\left(\frac{\partial A}{\partial r}\right)\right] \tag{3.1b}$$

where

$$U_{\rm Darwin} = \frac{1}{2E}\left[-\frac{1}{2r^2A}\frac{\partial}{\partial r}\left(r^2\frac{\partial A}{\partial r}\right) + \frac{3}{4A^2}\left(\frac{\partial A}{\partial r}\right)^2\right] \tag{3.2}$$

and

$$A = \frac{(E + U^S - U^V + M)}{(E + M)} \tag{3.3}$$

Fig. 4 compares the Schrödinger-like potential for ^{208}Pb from our model with the nonrelativistic Paris G-matrix calculation of Ref. [1]. The relativistic calculation gives

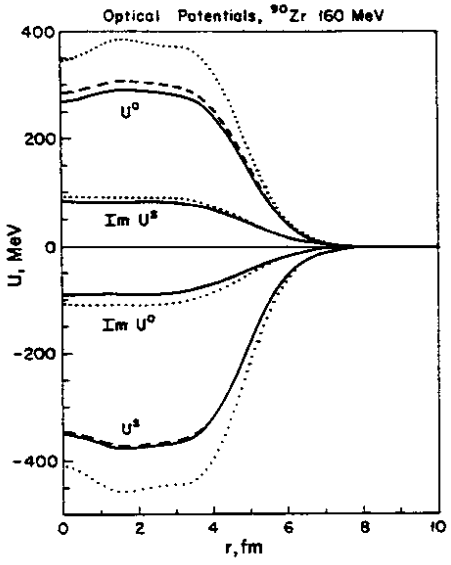

Fig. 2: Optical potentials for ^{90}Zr at 160 MeV. The dotted curves use pseudoscalar coupling without the Pauli blocking factor. The dashed curves use pseudovector coupling instead; the solid curves use pseudovector coupling and include the Pauli blocking factor.

a real central potential which is about 30 MeV more positive and has a non-Wood-Saxon shape, and a real spin orbit potential which is much stronger than the nonrelativistic result.

B. 200 MeV OBSERVABLES

In Figs. 5 through 10 we show the predictions of our model for the cross–section and spin observables A_y and Q for proton–nucleus scattering, at energies near 200 MeV. Experimental points, where available are also shown. The spin rotation, Q, data for ^{12}C, ^{16}O, ^{40}Ca, and ^{48}Ca are *preliminary* results from Indiana[20]. For the heavier nuclei ^{90}Zr and ^{208}Pb, Q has not yet been measured at 200 MeV. However, there is TRIUMF data for ^{208}Pb at 290 MeV.[21]

For our calculations, we have chosen pseudovector coupling for the "pion" of the model (for its contribution to the real optical potential). We have not included the small tensor potential in the scattering calculations (but see the discussion of ^{48}Ca below). For the baryon and scalar densities of Eqs. (2.27) and (2.29) we have used those of Horowitz and Serot[10]. The scattering observables calculated with these conventions

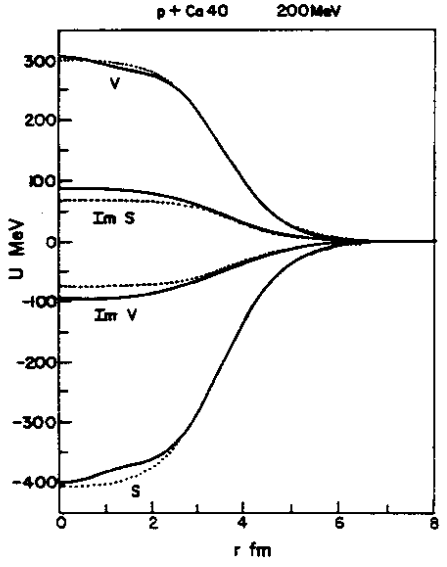

Fig. 3: Relativistic optical potentials for ^{40}Ca at 200 MeV. The solid curve is the microscopic calculation. The dotted curve is a phenomenological fit of Clark *et al.*[19]

are shown by the solid curves of Figs. 5 through 10 and Fig. 13. Total reaction cross sections for this set of calculations are given in Table III.

Generally, the calculations match the data quantitatively up to about 60°, beyond which there is some trouble with the magnitude of the cross sections and the phase of the spin observables. The spin observables A_y and Q are very well reproduced both in the magnitudes and phases of the oscillations. This agreement includes the forward angle region in Q where results are very sensitive to the optical potentials. Agreement is greatly improved over the original RIA without explicit exchange or Pauli blocking[7]. In Section IV we compare our results with other microscopic calculations.

Calculations for 300 MeV and 400 MeV are just as successful; some of these will be shown in part III.D.

C. SENSITIVITIES OF THE 200 MeV CALCULATIONS

We now look at at the importance of various features of the model in producing the good agreement with the data.

The most important single feature is the explicit treatment of nucleon exchange. In Figs. 10a and 13 we compare the full calculation for 200 MeV ^{208}Pb scattering (solid curve) with the original RIA using the MRW parametrization of F^S and F^V (dashed

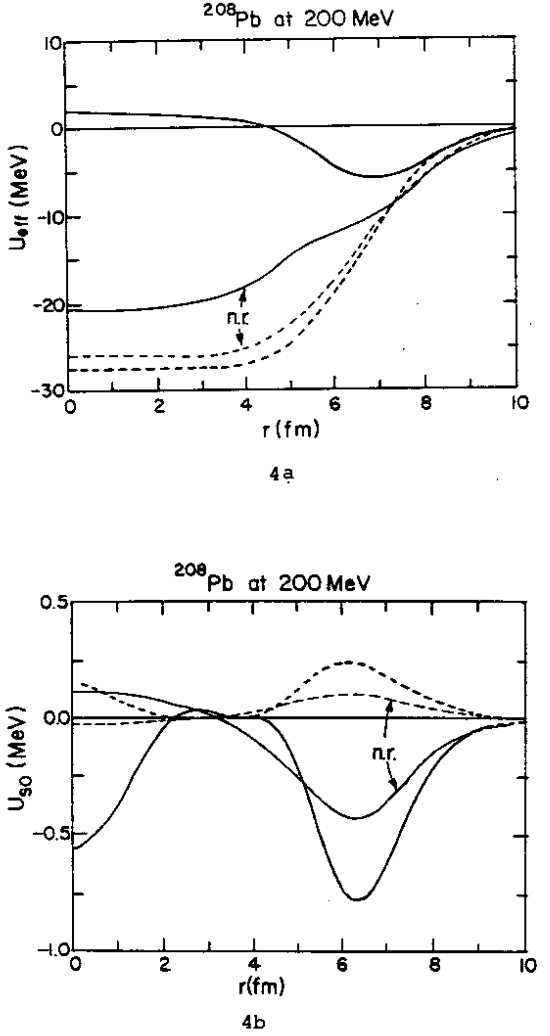

Fig. 4: Schrödinger potentials for ^{208}Pb at 200 MeV. Schrödinger-equivalent potentials, Eqs. (3.1a–3.3), from the relativistic calculation (heavy curves) are compared with the nonrelativistic (n.r.) results of von Geramb[1] (thin curves). Fig. 4a compares central and 4b compares spin–orbit potentials. Real potentials are solid and imaginary dashed curves.

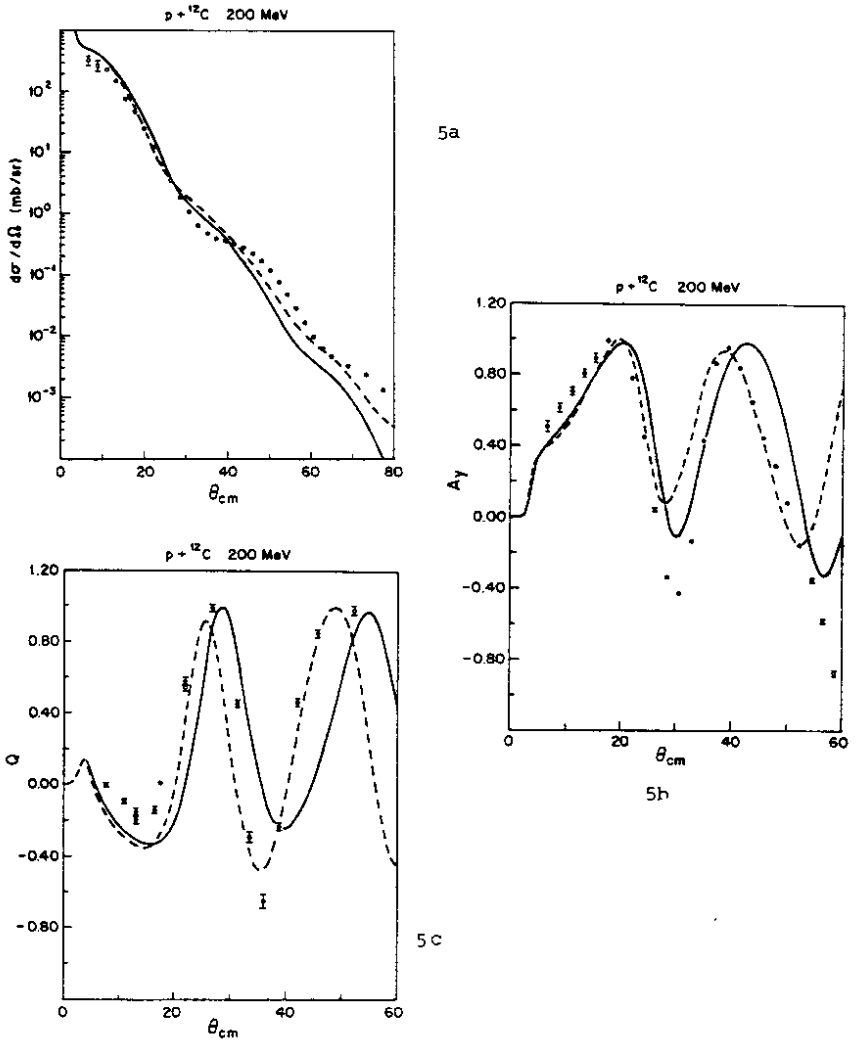

Fig. 5: Cross section (a), analyzing power (b) and spin rotation parameter (c) for 200 MeV ^{12}C scattering. The solid curves use Hartree densities. The dashed curves use empirical densities described in section III.C. Preliminary Q data is from Ref. [20].

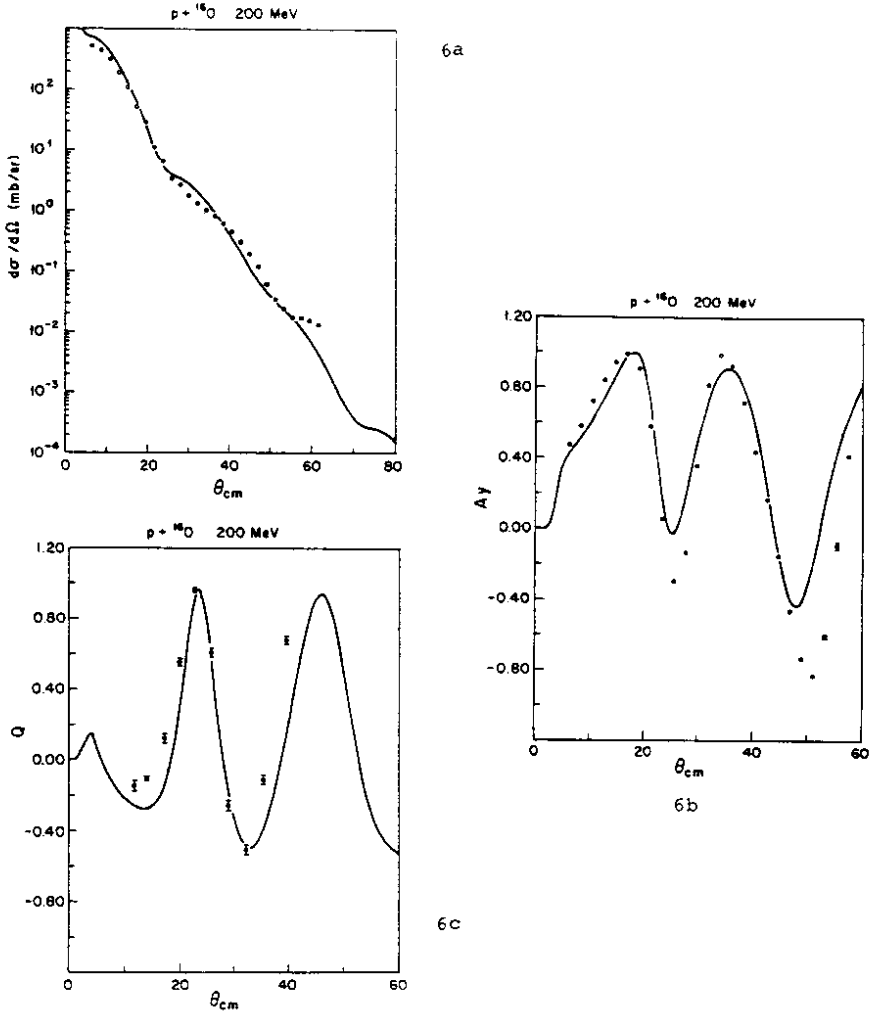

Fig. 6: Cross section (a), analyzing power (b) and spin rotation parameter (c) for 200 MeV ^{16}O scattering. Q data is from Ref. [20].

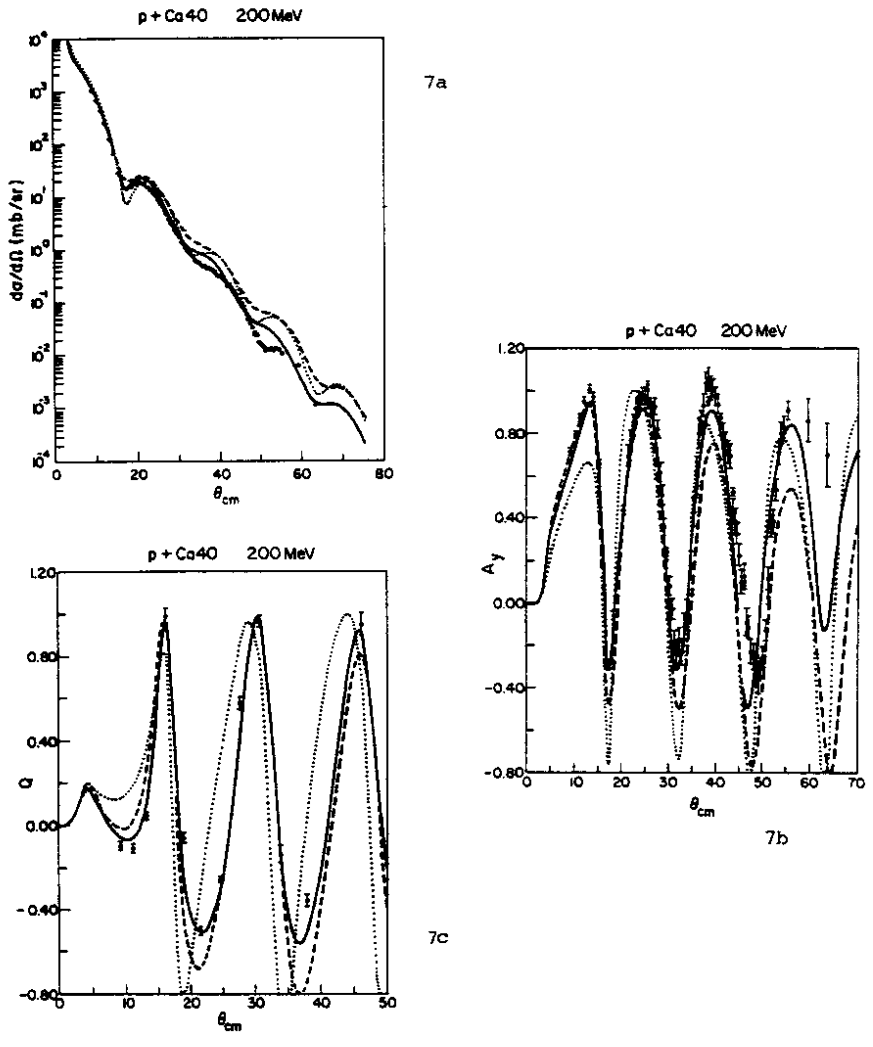

Fig. 7: Cross section (a). analyzing power (b) and spin rotation parameter (c) for 200 MeV ^{40}Ca scattering. The dashed curves use pseudoscalar coupling and include Pauli blocking. The dotted curves use pseudovector coupling but omit Pauli blocking. Data is from Ref. [20].

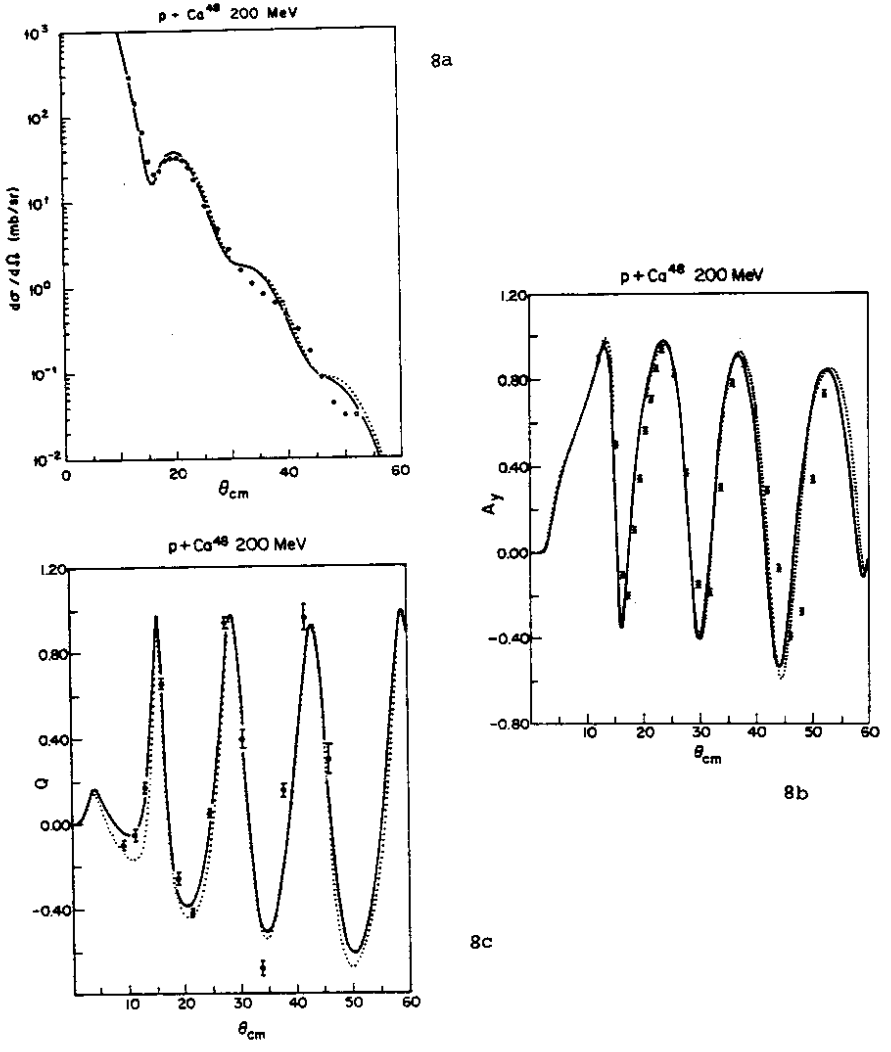

Fig. 8: Cross section (a). analyzing power (b) and spin rotation parameter (c) for 200 MeV ^{48}Ca scattering. The dotted curves include a small tensor potential. Data is from Ref. [20].

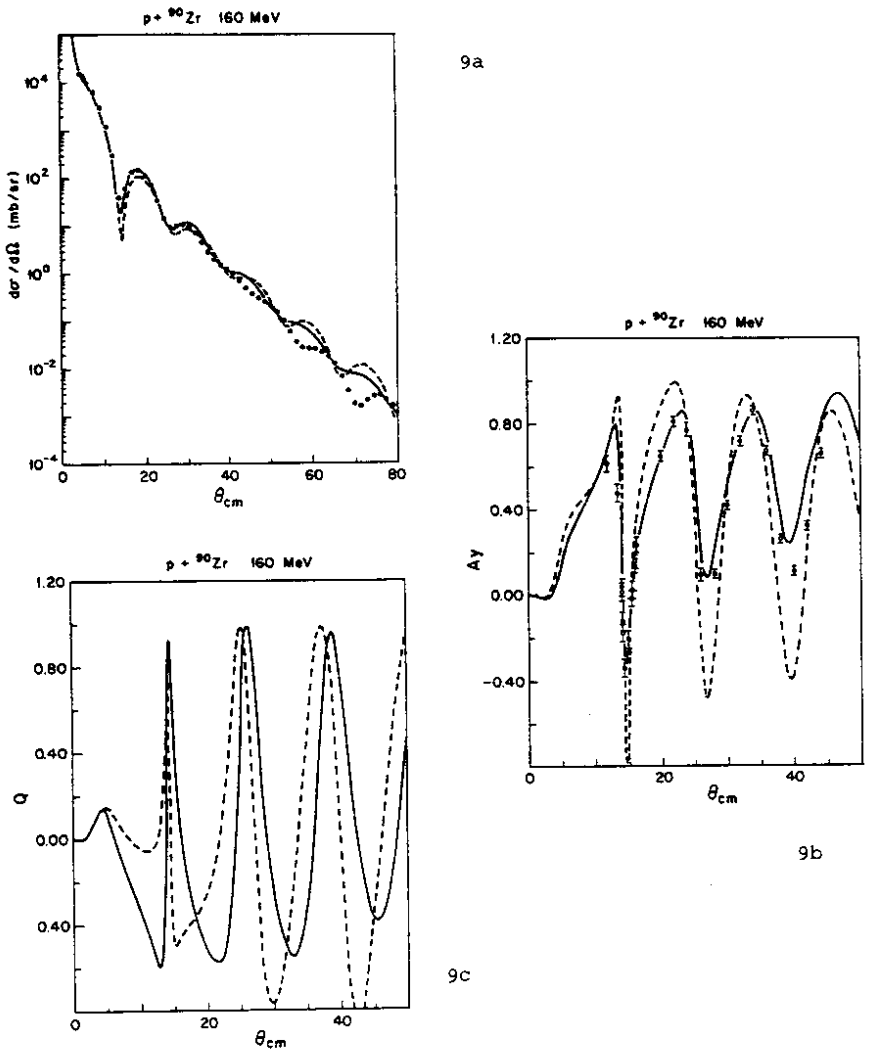

Fig. 9: Cross section (a), analyzing power (b) and spin rotation parameter (c) for 160 MeV ^{90}Zr scattering. The dashed curves use pseudovector coupling but omit the Pauli blocking correction. Data is from Ref. [33].

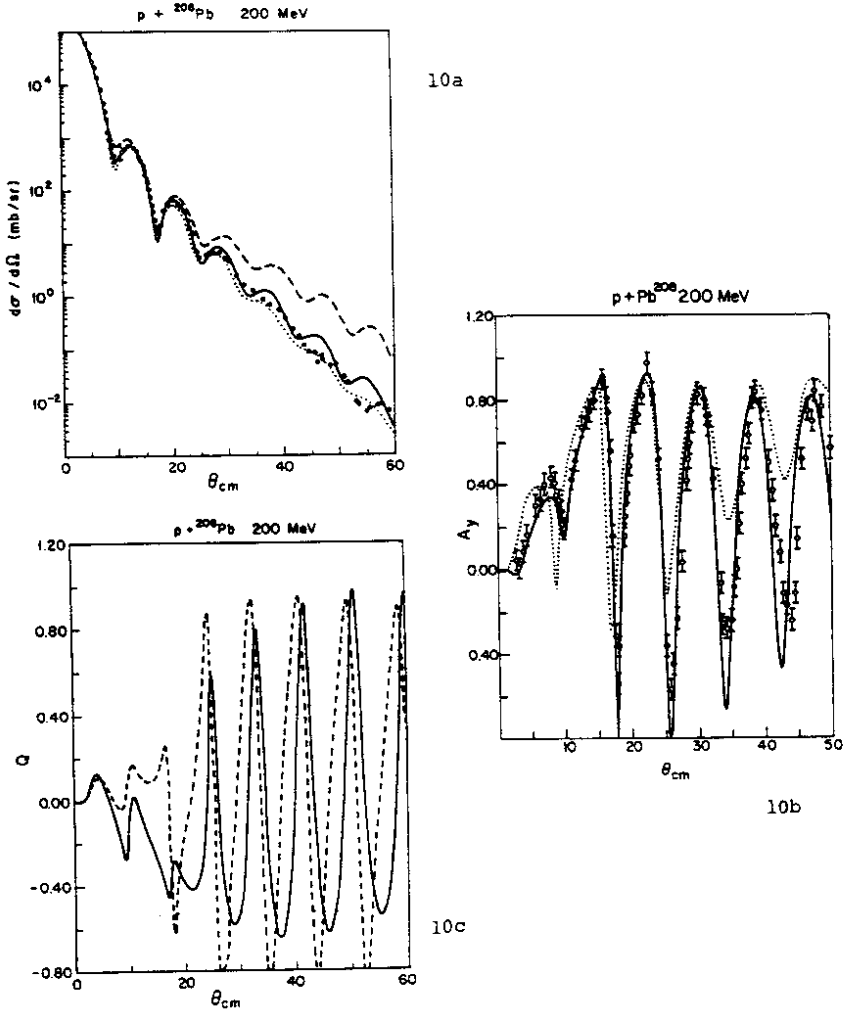

Fig. 10: (a) Cross section for 200 MeV ^{208}Pb scattering. The dashed curve is the original RIA calculation. The dotted curve differs from the solid curve in that empirical densities, described in Section III.C. are used. Data is from Ref. [31]. (b) Analyzing power for 200 MeV ^{208}Pb scattering. The dotted curve is the nonrelativistic calculation of Ref. [1]. Data is from Ref. [31]. (c) Spin rotation parameter for 200 MeV ^{208}Pb scattering. The dashed curve omits the Pauli blocking correction.

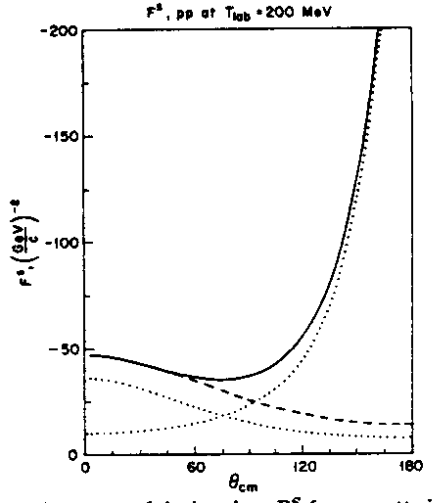

Fig. 11: Imaginary part of the invariant F^S for pp scattering at 200 MeV. The solid curve shows the values from the Arndt phase shifts[34]. The dashed curve is the MRW fit[4], extrapolated to large q. The F^S of our model is the sum of direct and exchange pieces which are respectively the decreasing and increasing dotted curves.

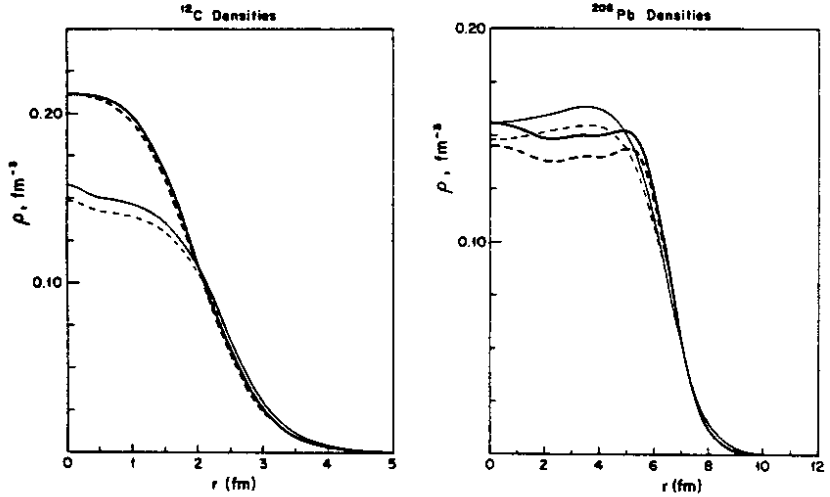

Fig. 12 Comparison of baryon and scalar densities for ^{12}C (a) and ^{208}Pb (b). from Hartree calculations and empirical sources described in the text. Solid curves are baryon densities and dashed curves are scalar densities. Heavy curves are from the Hartree calculation of Ref. [10]; thin curves are from empirical sources.

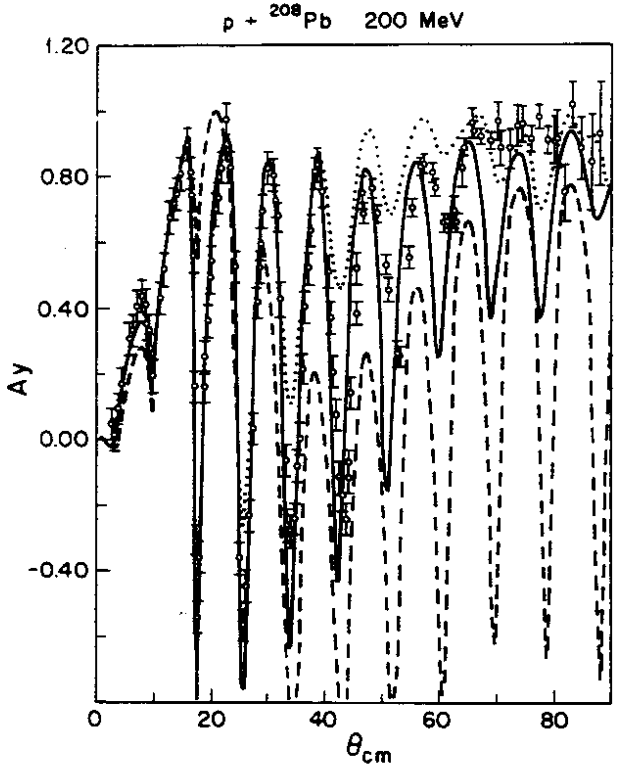

Fig. 13: Large–angle analyzing power for 200 MeV ^{208}Pb scattering. The dashed curve is the original RIA calculation. The dotted curve differs from the solid curve in that empirical densities for ^{208}Pb were used. Data is from Ref. [22].

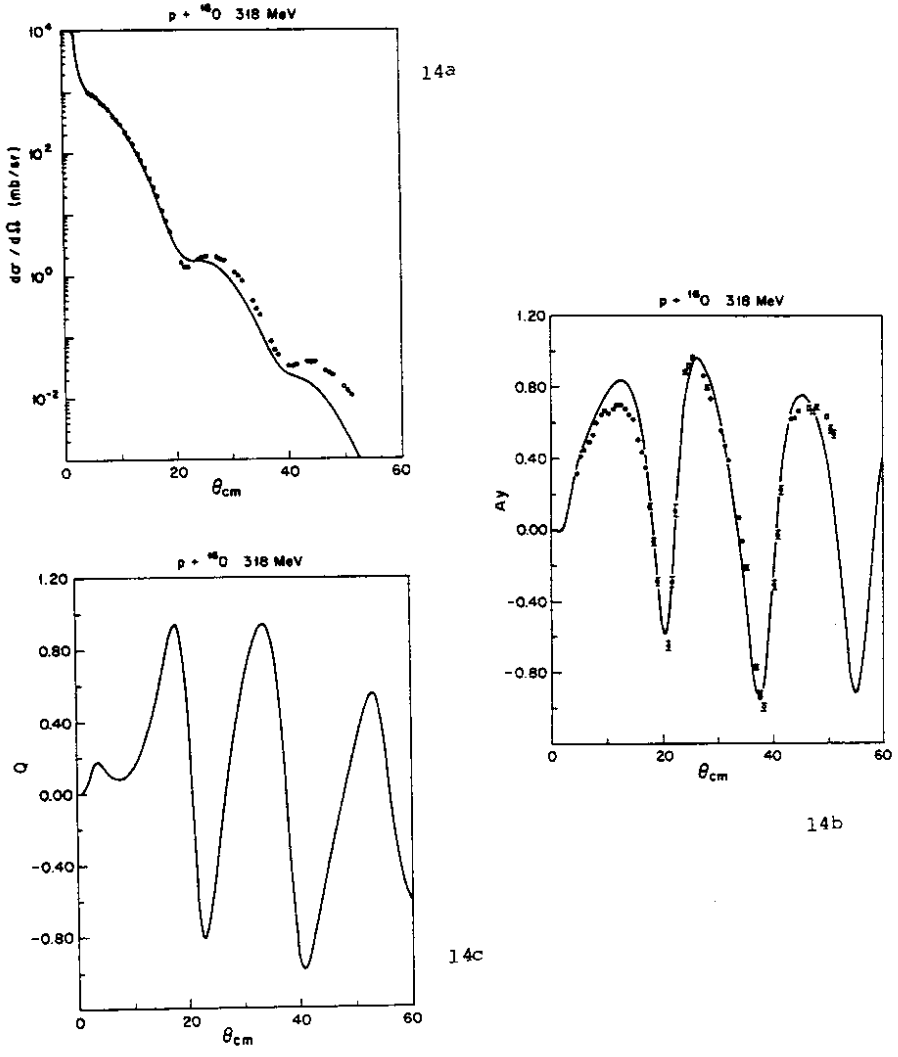

Fig. 14: Cross section (a), analyzing power (b) and spin rotation parameter (c) for 318 MeV ^{16}O scattering. Data is from Ref. [35].

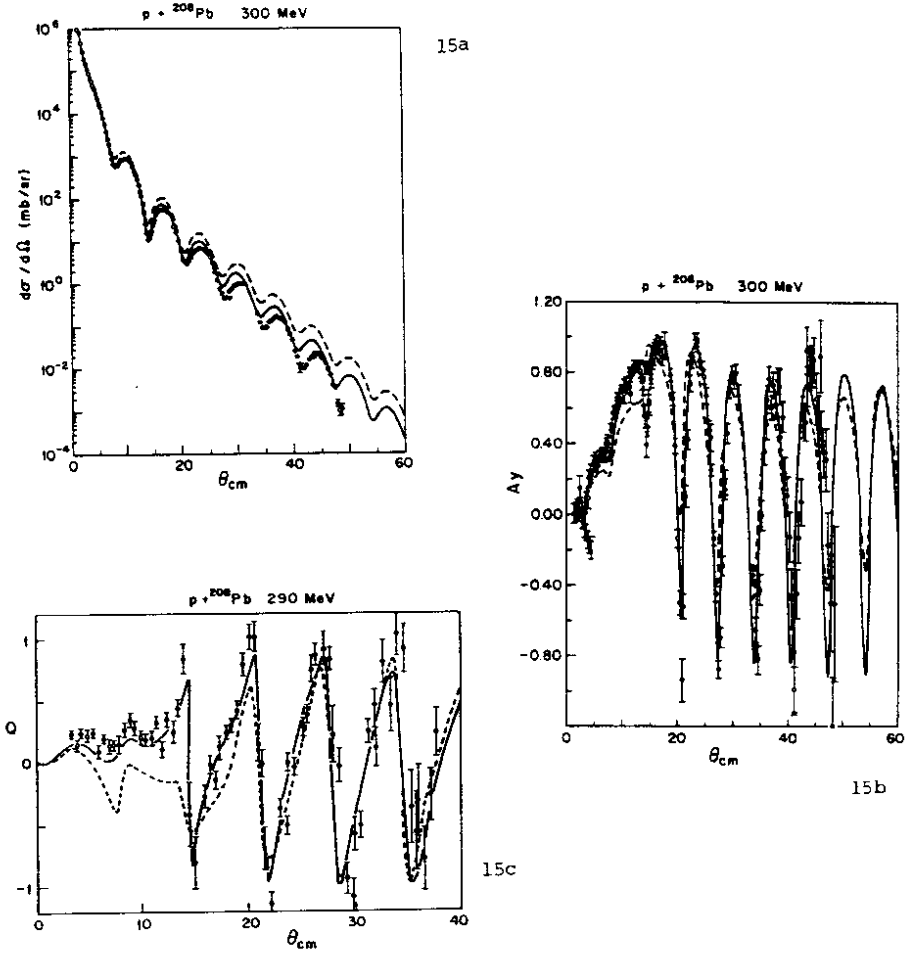

Fig. 15) Cross section (a), analyzing power (b) and spin rotation parameter (c) for 300 and 290 MeV ^{208}Pb scattering. The dashed curves in 15a and 15b omit the Pauli blocking correction. The dashed curve in 15c is a nonrelativistic calculation of Bauhoff *et al.*[26]. The TRIUMF data is from [21].

TABLE III		
Nucleus	$T_{\rm lab}$ (MeV)	$\sigma_{\rm total}$ (fm^2)
^{12}C	200	23.6
^{16}O	200	29.6
^{16}O	318	28.1
^{40}Ca	200	57.1
^{48}Ca	200	67.0
^{90}Zr	160	98.0
^{208}Pb	200	176.3
^{208}Pb	300	171.2
^{208}Pb	400	167.2

Total reaction cross sections for calculations with pseudovector coupling and Pauli blocking.

curve). (For the latter calculation, we have used new parameters for the pn invariants since there is an apparent misprint in the tables of Ref. [4].) The RIA is good only until about 30°, beyond which the cross section is too large and the analyzing power is far too negative. Our treatment of exchange brings both observables close to the data over a much larger range of scattering angles.

An explicit treatment of exchange is important because of the odd behavior of the MRW amplitudes under interchange of the two nucleons. In Fig. 11 we show the Lorentz scalar invariant F^S_{pp} at $T_{\rm lab} = 200$ MeV as a function of the NN center of mass scattering angle. Due to exchange contributions, F^S rises dramatically at large angles. Note that 60° scattering off of a heavy nucleus corresponds to 180° in the NN frame, so the amplitudes are needed at large angles.

The original RIA only fit the NN amplitudes up to *60 degrees in the NN frame*[3,4]. One such fit is shown if Fig. 11. However, for scattering from a heavy nucleus at nucleon-nucleus angles beyond $\approx$ 30°, the NN amplitudes are needed at much larger NN angles. Indeed, the MRW curve in Fig. 13 is very sensitive to the fit to the forward NN amplitude.

Thus the simple RIA with the original parametrization of the NN amplitudes is essentially calculating *random noise* for large nucleon-nucleus scattering angles. I.e. the RIA results for scattering beyond 60° depend solely on gross extrapolations of fits to the far forward NN amplitudes. Therefore, the conclusions in Ref. [22] about large angles are incorrect.

Note, the RIA calculations in Refs.[7] and [30] (but not those in Refs.[2].[3] or [22]) use the Breit frame prescription for the NN amplitudes. Here, NN amplitudes at the experimental $T_{\rm lab}$ and a large scattering angle are replaced by NN amplitudes at a higher effective $T_{\rm lab}$ and a smaller scattering angle (which gives the same momentum transfer). This somewhat alleviates the problem but at the cost of introducing unphysical reactive content into the NN amplitudes. For example, 200 MeV NN amplitudes can be replaced with up to 800 MeV amplitudes, which include unphysical pion production.

After the identification and local treatment of the exchange amplitude, we make a choice on the type of "pion" coupling used and include a rough treatment of Pauli blocking. Figs. 7a–7c show the cross section, A_y, and Q for ^{40}Ca at 200 MeV. The dashed curves differ from the calculation for the solid curves in that pseudoscalar coupling is used. The resulting cross section is too large. The dotted curves omit the Pauli blocking correction (but use a pseudovector pion) for which the cross section is too large and has too much structure. Furthermore, the spin observables disagree with the data at small angles.

Other comparisons of calculations with and without Pauli blocking (for ^{90}Zr and ^{208}Pb) are shown in Figs. 9, 10c, 15 and 16.

The small tensor potential was not included in the primary calculations for Figs. 5 through 10. Its small effect on the observables at 500 MeV has been demonstrated by Clark *et al.*[23]. It has a similar small effect at lower energies. Figs. 8a–8c show A_y and Q calculations for ^{48}Ca at 200 MeV. The solid curves use the same conventions as in the other figures while the dotted curves include the tensor potential (with a pseudovector pion coupling and no Pauli blocking factor for U^T). There is only a small change in Q at forward angles. The tensor potentials for ^{48}Ca are about twice as big as for ^{40}Ca because of the $f_{\frac{7}{2}}$ neutrons. Therefore, the effect of the tensor potential in ^{16}O and ^{40}Ca is even smaller than for ^{48}Ca.

Finally, there are sensitivities to the nuclear structure input. These must be taken into account before detailed comparisons are made with other models and the data at large scattering angles. We give examples of this uncertainty for 200 MeV ^{12}C and ^{208}Pb scattering. For ^{12}C we form an alternative baryon density by unfolding the proton charge form factor from the experimental carbon charge density. For ^{208}Pb we use the Gauss III parameters of Ref. [1] for the proton and neutron densities. Then we use a nuclear matter approximation to obtain the ratio of baryon to scalar densities. Our prescription, based on the relativistic mean field theory of Ref. [16] is to approximate $\rho_S = \left\langle \sqrt{1-\frac{v^2}{c^2}} \right\rangle \rho_B$ by

$$\rho_S(r) = \rho_B(r)\left(1 - \frac{3}{10}\frac{k_F^2}{M^{*2}}\right). \tag{3.4}$$

with k_F being the local Fermi momentum $k_F^3 = \frac{3\pi^2}{2}\rho_B$. Since at the saturation baryon density of .1934 fm^{-3}, the effective mass is $M^* = .56\,M$, we use a linear interpolation,

$$\frac{M^*}{M} \approx 1 - .44\frac{\rho_B}{.1934\ fm^{-3}}\ . \tag{3.5}$$

When the densities are calculated in this way for ^{12}C, proton and neutron densities are taken to be equal. Hartree densities for ^{12}C and ^{208}Pb are compared with these alternate densities in Fig. 12.

The differences in the resulting cross sections and analyzing powers for the choices of nuclear input are significant. For ^{12}C, the observables found from using the empirical

density are shown in Figs. 5a–5c by the dashed curves. Beyond 60° the phases of spin observables are very different.

For Pb, cross sections computed from the two sets of densities are likewise compared in Fig. 10a. The Hartree values are larger and have more structure at larger angles. Analyzing powers are compared in Fig. 13. Again, the two sets of densities give similar results at small angles, but beyond 50° there is much more structure in the Hartree curve. Clearly, any comparison of relativistic model predictions for large–angle spin observables must take into account the fine details of the target structure. In addition, vacuum fluctuations may significantly reduce ρ_S relative to ρ_B; see Ref. [24].

D. 300 MeV AND 400 MeV OBSERVABLES

The calculations for scattering at 300 MeV and 400 MeV are just as successful. Calculations for ^{16}O and ^{208}Pb for energies near 300 and 400 MeV are shown in Figs. 14, 15 and 16. The solid theoretical curves use the same model choices as for the 200 MeV calculations. (See Appendix A for the parameters used for the 300 MeV NN amplitudes.)

In the large nuclei Zr and Pb at 200 MeV and 300 MeV, Pauli blocking substantially changes Q (see Figs. 9c, 10c, and 15c) at forward angles. However, the only experimental data on the spin rotation parameter Q for either nucleus are for ^{208}Pb at 290 MeV [21]. They agree very well with the Pauli blocked calculation.

Even though the Pauli blocking effect for A_y is smaller at higher energies, its inclusion in our calculation gives a very noticeable change in A_y at forward angles, as shown in Fig. 15b, for 300 MeV and Fig. 16 for 400 MeV. The A_y values are moved up from the unblocked values to give agreement with experiment.

IV. OTHER MICROSCOPIC CALCULATIONS FOR 200 MeV

In this section we note some other work on microscopic calculations of optical potentials applicable to 200 MeV elastic scattering.

Tjon and Wallace[25] have performed a complete calculation of the invariant amplitude $\hat{\mathcal{F}}$ [9]. Within their model for the NN interaction, there is no further ambiguity in the form of $\hat{\mathcal{F}}$. The $\hat{\mathcal{F}}$ matrix elements were calculated using NN data for the positive energy free spinor matrix elements and a meson model for the rest. Pseudovector coupling is used for the pion to insure that the pion–exchange contribution to the optical potential is well-behaved. However, Ref. [25] presents results for the potentials and scattering observables without any correction for Pauli blocking as in our Eq. (2.35). An important additional difference with our work is that they do not make the separation into direct and exchange invariants, and so they do not use the particular kinematics which are built into the tp folding for each part, described in Section II.C.

The spin observables for ^{40}Ca which they calculate agree with the data about as well as our results, while the cross sections are too large beyond $\approx 30°$, probably due to the omission of Pauli blocking and an explicit treatment of exchange. It would be interesting to see their calculations for ^{208}Pb where we find large Pauli blocking effects.

The nonrelativistic calculation of Rikus and von Geramb[1] used an effective interaction (nonrelativistic, with central and spin–orbit pieces) generated from a Brueckner

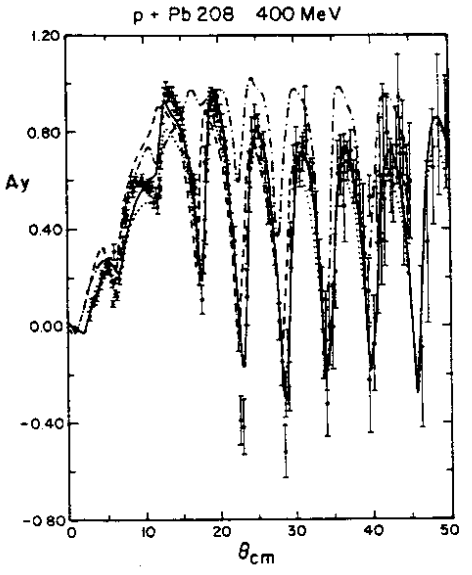

Fig. 16: Analyzing power for 400 MeV ^{208}Pb scattering. The solid curve includes Pauli blocking while the dotted curve does not. The nonrelativistic calculation with medium modifications[1] is dashed, while the dot–dashed curve is the nonrelativistic KMT impulse result of Ref. [7]. The TRIUMF data is from Ref. [32].

calculation using the Paris potential. Pauli blocking is thus built into the interaction from the beginning. Also, since they begin with a model t–matrix, they make the separation into direct and exchange parts and then do the folding with the nonrelativistic densities as we do in Eqs. (2.27) and (2.29). The agreement with the Pb data for cross sections and polarizations is good except for the small angle values of the polarization, where nonrelativistic calculations typically miss the second minimum. However, for Q, there are larger differences. In Fig. 15c we show the calculation of Bauhoff[26] for ^{208}Pb at 290 MeV. Here, the nonrelativistic calculation has the wrong sign for Q at forward angles ($\leq 15°$).

Nonrelativistic impulse approximation calculations[7] give poor spin observables near 200 MeV. Although the medium–modified nonrelativistic calculations do much better in certain cases (for example, ^{40}Ca [27]), there are no published nonrelativistic results which systematically reproduce all the spin observables shown here.

We do not claim our good relativistic description is unique. Some nonrelativistic calculations have also reproduced selective spin observables. It would be useful to have

a systematic series of nonrelativistic calculations of all 200 MeV spin observables.

These relativistic calculations have smaller Pauli blocking corrections than in nonrelativistic works. It is an important open question to further understand the role of relativity and/or medium modifications in giving good agreement with data.

Thies[28] has claimed that the *non*relativistic propagator is badly behaved at short distances. Thus, he postulates that if short–ranged correlations are included, the final results will be less sensitive to this short–distance problem. However, Cooper and Jennings[29] have estimated a short distance correlation parameter and find its effects to be much too small. Furthermore, the medium modifications in Ref. [1] may be quite different from Thies's correlations. Thus, there are many open questions in comparing relativity and/or medium modifications.

V. CONCLUSIONS

We have presented a new formalism for calculating relativistic optical potentials for elastic proton scattering from closed shell nuclei. This formalism contains important physics not in the original relativistic impulse approximation.

First, exchange terms are explicitly included in the optical potential. This allows one to deal with the dramatic increase of the relativistic NN amplitudes at large scattering angles. A proper treatment of exchange is crucial for describing large angle analyzing power and cross section data.

Next, ambiguities in the relativistic form of the NN amplitude are resolved by using a pseudovector coupling for the pion. This reduces both the strength and energy dependence of the real scalar and vector optical potentials.

Finally, medium modifications from Pauli blocking are incorporated using relativistic Brueckner results for nuclear matter in a local density approximation. Pauli blocking reduces the imaginary optical potential.

Calculations for ^{12}C, ^{16}O, ^{40}Ca, ^{48}Ca, ^{90}Zr and ^{208}Pb at $T_{\rm lab}$=200 MeV including these three corrections *quantitatively* reproduce all measured elastic spin observables. Both the analyzing power and spin rotation function are reproduced out to about 60 degrees. If Pauli blocking is omitted or if pseudoscalar pion coupling is used, the spin observables are significantly worse. In particular, Q for ^{208}Pb at 290 MeV changes dramatically if Pauli blocking is omitted.

The energy dependence of these corrections has been examined with calculations at $T_{\rm lab}$ = 300 and 400 MeV. As $T_{\rm lab}$ increases, the importance of Pauli blocking diminishes. At 400 MeV in ^{208}Pb, Pauli blocking has a much smaller effect on A_y than do medium modifications in nonrelativistic calculations.

Also, the difference between pseudoscalar and pseudovector amplitudes is not important at $T_{\rm lab}$ = 400 MeV. Furthermore, current experimental data does not extend to large enough angles for an explicit treatment of exchange to be crucial. Therefore, these calculations essentially agree with the original RIA at $T_{\rm lab}$= 500 MeV and above.

Much theoretical work needs to be done to get a formalism which is satisfactory at still lower energies and for larger scattering angles. This will require more detailed calculations of Pauli blocking, the resolution of other ambiguities in the NN amplitudes and more constraints on the target densities.

Finally, it would be useful to complete the 200 MeV data set with spin rotation parameter measurements for ^{90}Zr and ^{208}Pb. For these nuclei we find large Pauli blocking effects at forward angles.

ACKNOWLEDGEMENTS

T. Drake, O. Hausser and E. Stephenson are thanked for providing preliminary experimental data.

REFERENCES

1. L. Rikus and H.V. von Geramb, *Nucl. Phys.* **A426**, 496 (1984).
2. J. A. McNeil, J. R. Shepard and S. J. Wallace, *Phys. Rev. Lett.* **50**, 1439 (1983).
3. J. R. Shepard, J. A. McNeil and S. J. Wallace, *Phys. Rev. Lett.* **50**, 1443 (1983).
4. J. A. McNeil, L. Ray, and S.J. Wallace, *Phys. Rev.* **C27**, 2123 (1983).
5. D. L. Adams and M. Bleszynski, *Phys Lett.* **136B**, 10 (1984).
6. C. J. Horowitz, *Phys. Rev.* **C31**, 1340 (1985).
7. L. Ray and G. W. Hoffman, *Phys. Rev.* **C31**, 538 (1985).
8. T. Drake in *Medium Energy Nucleon and Antinucleon Scattering*, edited by H. V. von Geramb, Bad Honnef, West Germany 1985, Springer–Verlag.
9. J. A. Tjon and S. J. Wallace, *Phys. Rev.* **C32**, 1667 (1985).
10. C. J. Horowitz and B. D. Serot, *Nucl. Phys.* **A368**, 503 (1981).
11. C. A. Miller *et al.*, *Phys. Lett.* **169B**, 166 (1986).
12. C. J. Horowitz and J. Iqbal, *Phys Rev.* **C33**, June (1986).
13. J. D. Bjorken and S. Drell, *Relativistic Quantum Mechanics*, (McGraw-Hill, New York) 1965.
14. K. Holinde and R. Machleidt, *Nucl. Phys.* **A247**, 495 (1975).
15. K. Holinde, K. Erkelenz and R. Alzetta, *Nucl. Phys.* **A194**, 161 (1972).
16. Brian D. Serot and J. D. Walecka in *Advances in Nuclear Physics*, edited by J. W. Negele and E. Vogt, Vol. 16.
17. F. A. Brieva and J. R. Rook, *Nucl. Phys.* **A291**, 317 (1977).
18. C. J. Horowitz and B. D. Serot, submitted to *Nucl. Phys. A*.
19. B. C. Clark, S. Hama and R. L. Mercer in *The Interaction Between Medium Energy Nucleons in the Nucleus*, edited by H. O. Meyer, p. 260.
20. E. J. Stephenson in *Antinucleon– and Nucleon–Nucleus Interactions*, Telluride, Colorado, March 1985, edited by G. E. Walker *et al.*, Plenum Press 1985.
21. O. Hausser *et al.*, to be published.

22. T. Drake in *Medium Energy Nucleon and Antinucleon Scattering*, Bad Honnef, West Germany, June 1985, edited by H. V. von Geramb, Springer–Verlag 1985.

23. B. C. Clark *et al.*, *Phys. Rev. Lett.* **51**, 1808 (1983).

24. C.J. Horowitz and Brian D. Serot, *Phys. Lett.* **140B**, 181 (1984).

25. S. J. Wallace, *Proceedings of the LAMPF Workshop on Dirac Approaches to Nuclear Physics*, edited by J. R. Shepard, C. Y. Cheung and R. L. Boudrie, LA 10438–C.

26. W. Bauhoff, private communication and in *Medium Energy Nucleon and Antinucleon Scattering*, Bad Honnef, West Germany, June 1985, edited by H. V. von Geramb, Springer–Verlag 1985.

27. W. Bauhoff, *Phys. Rev.* **C30**, 1113 (1984).

28. M. Thies, *Phys. Lett.* **162B**, 255 (1985).

29. E. D. Cooper and B. Jennings, submitted to *Phys. Rev. C*.

30. B. C. Clark, S. Hama, R. L. Mercer, L. Ray, and B. D. Serot, *Phys. Rev. Lett.* **50**, 1644 (1983).

31. D. A. Hutcheon *et al.*, *Polarization Phenomena in Nuclear Physics*, G. G. Ohlsen, ed., (1980) (AIP.1981).

32. D. A. Hutcheon *et al.*, *Phys. Rev. Lett.* **47**, 315 (1981).

33. P. Schwandt *et al.*, *Phys. Rev.* **C26**, 55 (1982).

34. R. A. Arndt and D. Roper, VPI and SU Scattering Analysis Interactive Dial-In Program and Data Base.

35. M. Hynes *et al.*, private communication.

APPENDIX A

The values of the coupling constants g^2 listed in Ref. [6] were flawed by an inconsistent normalization of the free Dirac spinors; this has been corrected in Section II of this work. To make Ref. [6] consistent, multiply the right sides of equations (5) and (18) through (20) by $\frac{M^2}{E_c^2}$ and the listings for g^2 by the appropriate numerical values of $\frac{E_c^2}{M^2}$. With this correction, the π, σ, and ω couplings show even less variation with energy and are closer to the OBEP values.

This changes only the values of g^2 in [6] and not the NN observables calculated from the parameter fits or their comparison with the Arndt amplitude predictions.

For the 300 MeV optical potentials calculated for ^{16}O and ^{208}Pb we have used parameters for a 10–meson fit to the Arndt amplitudes, given in Table IV. The notation used is the same as in Ref. [6] except that the values of g^2 now include the correction. The NN observables calculated from this fit are not as close to the Arndt predictions as those in Ref. [6] and this 300 MeV fit should be considered preliminary. The Pauli blocking parameters a_i for 300 MeV were found by interpolating the 200 and 400 MeV values.

TABLE IV

			Real			Imaginary		
Meson	Isospin	Lorentz Type	m	g^2	Λ	$\bar{m}$	$\bar{g}^2$	$\bar{\Lambda}$
π	1	P	138	13.33	577.43	500	-2.205	473.95
η	0	P	550	3.391	2500	1000	4.989	2500
σ	0	S	500	-5.861	1008.2	600	-1.807	724.66
ω	0	V	783	9.825	862.17	700	2.948	685.89
t_1	1	T	600	0.122	650.57	750	0.066	2427.16
a_1	1	A	800	-.556	388.83	1000	0.049	200
δ	1	S	960	-.002	200	650	1.655	631.8
ρ	1	V	760	-.385	647.04	600	-1.258	633
t_0	0	T	800	0.006	200	750	-.356	691.1
a_0	0	A	1275	0.190	719.74	750	-.898	762.61

Meson parameters for $T_{\rm lab} = 300$ MeV. Parameters m, $\bar{m}$ and Λ, $\bar{\Lambda}$ are in MeV.

For the optical potentials calculated for proton lab energies near 200, 300 and 400 MeV we have simply used the model parameters found for the latter values without a complete refitting to the NN data.

APPENDIX B

The computer code used to generate the scattering observables in Section III solves the "Schrödinger equivalent" equation, a second order differential equation for the upper components of the Dirac wavefunction for the projectile. The most important terms for the equivalent potential were given in Eqs. (3.1)–(3.3). See also Ref. [19]. A prescription for treating center–of–mass motion is required in order to define the quantities M and E in these expressions. We choose M to be the rest mass of the proton and E to be the (total) energy of the projectile in the proton–nucleus center–of–mass frame:

$$E \equiv E_{p,\mathrm{cm}} = \frac{M^2 + M_T(M + T_{\mathrm{lab}})}{\sqrt{(M + M_T)^2 + 2M_T T_{\mathrm{lab}}}} \qquad (B.1)$$

where M_T is the mass of the target. When other (similar) choices are made, there is a small but noticeable change in the observables, especially for scattering from ^{12}C and ^{16}O. A systematic treatment of "recoil", or $\frac{1}{A}$ corrections remains to be done for relativistic systems.

We make the following approximations for the Coulomb interaction: The charge density of the target is taken to be that of a uniformly charged sphere of radius $r_0 A^{\frac{1}{3}}$ with $r_0 = 1.25\ fm$. Nonrelativistic Coulomb wavefunctions are used for the matching condition at large r. The observables are not sensitive to these choices.